

Article

Extension of Ship Wake Detectability Model for Non-Linear Influences of Parameters Using Satellite Based X-Band Synthetic Aperture Radar

Björn Tings , Andrey Pleskachevsky, Domenico Velotto  and Sven Jacobsen 

German Aerospace Center, Henrich-Focke-Str. 4, 28199 Bremen, Germany; andrey.pleskachevsky@dlr.de (A.P.); domenico.velotto@dlr.de (D.V.); sven.jacobsen@dlr.de (S.J.)

* Correspondence: bjoern.tings@dlr.de

Received: 29 January 2019; Accepted: 25 February 2019; Published: 7 March 2019



Abstract: The physics of the imaging mechanism underlying the emergence of ship wakes in Synthetic Aperture Radar (SAR) images has been studied in the past by many researchers providing a well-understood theory. Therefore, many publications describe how well ship wakes are detectable on SAR under the influence of different environmental conditions like sea state or local wind, ship properties like ship speed or ship heading, and image acquisition parameters like incidence angle or satellite heading. The increased imaging capabilities of current satellite SAR missions facilitate the collection of large datasets of moving vessels. Such a large dataset of high resolution TerraSAR-X acquisitions now enables the quantitative analysis of the previously formulated theory about the detectability of ship wakes using real data. In this paper we propose an extension of our wake detectability model by using a non-linear basis which allows consideration of all the influencing parameters simultaneously. Such an approach provides new insights and a better understanding of the non-linear influence of parameters on the wake detectability and their interdependencies can now be represented. The results show that the non-linear, interdependent influence of the different influencing parameters on the detectability of wakes matches well to the oceanographic expectations published in the past. Also possible applications of the model for the extraction of missing parameters and automatic for wake detection systems are demonstrated.

Keywords: Wake detection; Synthetic Aperture Radar; support vector machines; detectability model

1. Introduction

The detection of ships on space-borne Synthetic Aperture Radar (SAR) imagery is hardly possible, when the ship's construction material is non-conductive and in turn the ship's SAR-signatures are not or badly represented in the SAR images [1]. Instead of searching for the signatures of ships directly, their presence can be determined indirectly through the ship's wakes [2]. Since the automatic detection of ships on SAR has become of interest in earth observation, also the automatic detection of wakes is taken into account [3]. However, the maturity of automatic ship detection methods is further developed than of automatic wake detection methods, what is also reflected by the diverging amount of publications proposing different methods for the detection approaches [4–9].

A similar context can also be observed in the existence of approaches for modeling the detectability of ship or wake signatures in dependency to parameters influencing their detectability in SAR imagery. In the following these parameters will be called influencing parameters. While different approaches for modeling ship detectability have been published in past years and tuned for various SAR missions [10–13], a model for the detectability of wake signatures using real data has only been published recently [14]. However, theoretical assumptions about the dependency of influencing

parameters with the detectability of certain components of wakes using simulated data and physical contemplations exist since decades [15]. The well-known effects of tilt modulation, hydrodynamic modulation, and velocity bunching are the basis for general theories about the emergence of ocean surface waves and their visibility on SAR imagery [16–18].

SAR signatures of ship wakes are categorized into the four main wake components: turbulent wake, narrow V-wakes, ship-generated internal waves, and the Kelvin wake pattern [19]. The turbulent wake consists of a rough sea region (white water) up to two ship beams aft the ship induced by the propeller and a calm sea region beginning after it and persisting up to tens of kilometers caused by the attenuation of ambient short surface waves by ascending bubbles and surfactants. The rough sea region is responsible of high radar backscatter due to the strong turbulence and breaking waves while the calm sea region is responsible of low radar backscatter due to the smoothed surface [20–22]. By turbulent wake in this study we only refer to the long and smooth region, as the white water region is observable almost independently from the influencing parameters and easily confused with the ship signature itself. The Kelvin wake pattern consists of transverse, divergent, and cusp waves [23]. The cusp waves lie on the Kelvin wake arms and constitute the dominant backscattering responsible for the detectability of the V-shaped Kelvin envelope [15,19]. In this study only high resolution SAR data acquired from the TerraSAR-X satellite at a center frequency of 9.65 GHz (X-band) is used. Therefore, the narrow V-wakes cannot be taken into account as their half angle on X-Band is so small that they are expected being consumed by the turbulent wake [19,24,25]. According to [26] the visibility of Bragg-based scattering generated by both narrow V-wakes and ship-generated internal waves depends on variety of mechanisms making them also difficult to discriminate. Indeed, Bragg waves can be modulated by ship-generated internal waves on the ocean surface making them also visible on X-Band [27], but their emergence depends among other things on the water depth and the presence of either surface films or interactions with surface currents [19,28]. These kinds of influences can neither be derived from SAR automatically nor be provided by oceanographic models in adequate resolution. The requirement for a large dataset in this study only permits the consideration of influencing parameters which are automatically derivable. This means internal waves cannot be regarded appropriately and the scope of this study is restricted to the detectability of only two main wake components: turbulent wake and Kelvin wake.

Literature is rich in publications describing the dependency of influencing parameters with the detectability of turbulent wake and Kelvin wake. Most of the conclusions are in good agreement with each other. The following paragraphs are dedicated to reviewing previous studies about detectability of ship wakes in dependency to the influencing parameters investigated in this study.

Lyden et al. [19] state that the whole Kelvin envelope is best detectable when observed in alignment with the azimuth direction, and the individual cusp waves are better visible when traveling into range direction. This statement is also supported by [15] and [23], while in [15] it is pointed out that cusp waves propagating towards the radar-looking direction show an increase in backscatter relative to the surrounding and cusp waves propagating away from the radar-looking direction show a decrease in relative backscatter. Lyden et al. [19] further suggest that for turbulent wakes the relative-looking direction to the ship track is less influencing, but a relative looking direction perpendicular to the ship track produces the best results.

In [19] the authors pointed out that turbulent wakes and Kelvin wakes are best visible under moderate wind conditions, i.e. wind speed in the value range 2.5–10 m/s [22]. Hence, the minimum wind speed considered in this study is 2 m/s being also the minimum wind speed retrievable from SAR imagery [29], and the maximum wind speed is 10 m/s. Hennings et al. [15] describe that the Kelvin wake arms are better visible with lower wind speeds, as the contrast between cusp waves and background sea surface roughness decreases under the influence of higher wind speeds. Additionally, an outcome of the analysis conducted in [15] is the low dependency of detectability of Kelvin wake arms to relative wind direction.

In [30] the author suggests that signatures of turbulent wakes are visible also under moderate sea state conditions due the destruction of the ambient wind-generated waves by the wake's currents, although their extent is larger in low sea state conditions. This is confirmed by Tunaley et al. [24] at least for large vessels. Additionally, wakes generated by large vessels with slow velocities would further be visible under low sea state conditions and azimuthal wind direction. Reference [24] further stated that the Kelvin wakes are less visible in high sea state conditions and proposed that velocity bunching produced by transverse waves is responsible for this. The worse detectability of turbulent and Kelvin wakes in high sea state conditions is also confirmed by Zilman et al. [18].

Kelvin wakes are expected being better visible in HH-polarized images compared to VV-polarized images [15,23]. For the turbulent wakes no definite conclusion about the difference regarding HH and VV polarization was found in the literature, but the SAR imaging of water surfaces smoothed by the turbulent wakes is similar compared to water surfaces smoothed by oceanic surface films. For oceanic surface films, Gade et al. [31] found that there is no significant difference between detectability on HH- or VV-polarized images. A slightly better total detectability on HH images compared to VV images was also found by [14,21]. As the difference in dependency of detectability to influencing parameters is insignificant, HH and VV are not distinguished in this study.

The influence of the radar's incidence angle on wake detectability is similar for turbulent and Kelvin wakes. While [15] states that the detectability of Kelvin wake arms decreases, when the incidence angle increases, according to [32] the detectability of smoothed ocean surfaces, such as turbulent wakes, also decreases with increasing incidence angle.

The model we proposed in [14] only takes three influencing parameters into account at a time and assumes a linear dependency between the influencing parameters and the detectability of wakes. Especially for influencing parameters with units measured by degree, a linear model basis is assumed insufficient. Further, all influencing parameters must be considered simultaneously in one model in order to obtain comparable probability of detection estimates. This paper presents results achieved using a model with higher complexity and able to take into account all the influencing parameters introduced in [14] together. Besides these influencing parameters, additional influencing parameters are included and evaluated. Finally, possible applications of the extended wake detectability model are demonstrated.

2. Materials and Methods

The flow-chart in Figure 1 displays the overall procedure divided in three main steps: Extraction of labelled wake samples (Figure 1A); extraction of the influencing parameters from these samples (Figure 1B); and building of the detectability model and its visualization (Figure 1C). The first two steps are fully described in the remainder of this section while the third step deserves a dedicated section which follows-on.

The data used in this study is based on a dataset of 791 high resolution TerraSAR-X scenes acquired between the years 2013 to 2017 in North Sea, Baltic Sea and Mediterranean Sea. The scenes were acquired in Stripmap or Spotlight mode mostly with HH-polarization (in detail: 530 HH-polarized, 81 VV-polarized and 180 dual-co-polarized images). For all images, at least one ship's self-reporting message via the Automatic Identification System (AIS) was available. AIS provides information about ship properties like speed over ground or vessel location, which were used as influencing parameters as well as to identify possible locations of wake signatures. For the latter, an automatic intersection of AIS with the SAR images was executed to assign AIS messages to image regions. A manual correction of these colocations was performed to let the unreliable AIS data fulfill ground truth requirements, which means colocations have been discarded in case of large amounts of artifacts like ambiguities or marine objects being present. Then on the basis of these two datasets co-located in space and time a manual search for moving vessels was conducted (Figure 1(A.1)). During the search the background of the moving vessels was checked for unambiguous visibility or non-visibility of wake signatures.

By doing so to each wake sample either the class label “detected” or “not detected” was assigned (Figure 1(A.2)). Detailed information about the manual inspection procedure can be found in [14].

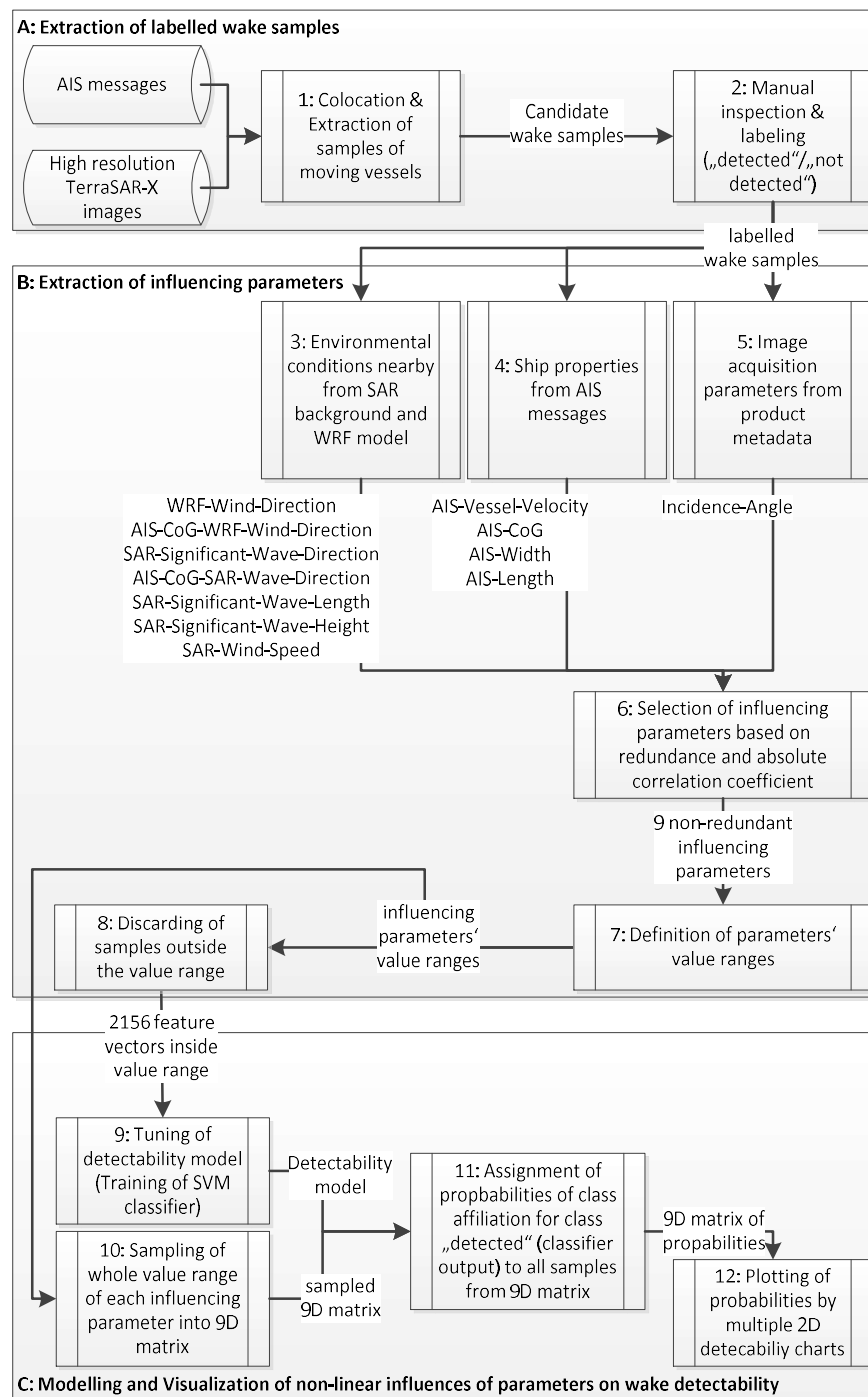


Figure 1. Flow-chart describing the overall process from data preparation (A) over retrieval of relevant parameter influencing the detectability (B) up to building of the detectability model and its visualization (C). AIS: Automatic Identification System; SAR: Synthetic Aperture Radar.

The detectability of wake signatures is affected by a number of influencing parameters (Figure 1(B.3),(B.4),(B.5)). A comparison of Pearson product-moment correlation coefficients was conducted in order to select influencing parameters with distinct physical background. The correlation coefficients are calculated for each influencing parameter between the parameter's magnitudes of

all wake samples and their respective class labels, where “detected” was quantified as 1 and “not detected” as 0. Figure 2 shows a graph with all twelve compared influencing parameters and their absolute correlation scores. From influencing parameters with redundant physical background the respective influencing parameters with lower absolute correlation score were discarded (Figure 1(B.6)). The discard applies to the following three redundant influencing parameters: WRF-Wind-Direction, which describes the relative wind direction from the Weather Research and Forecasting Model (WRF) towards the radar beam, SAR-Significant-Wave-Direction, which describes the relative wave direction towards the radar beam, and AIS-Width, which defines the width of the ship producing the wake.

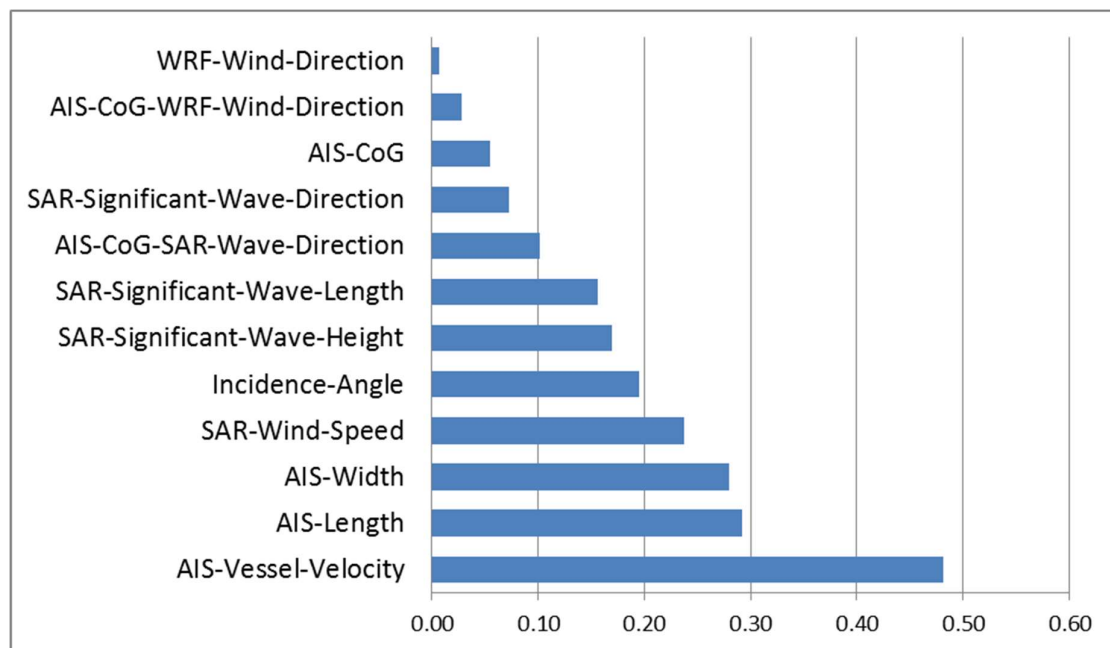


Figure 2. Plot of absolute correlation coefficients (Pearson product-moment correlation coefficients) of each influencing parameter with the wake visibility used for selection of parameters with distinct physical background. WRF: Weather Research and Forecasting Model.

A description of the remaining nine influencing parameters can be found in Table 1. It was decided to not apply any further dimensionality reduction technique as a meaningful, distinct physical background of the influencing parameters is supposed to be more important than expressive or independent parameters. Extreme characteristics of the influencing parameters only rarely occur in reality, e.g., small ships can hardly travel at high wind speeds and sea state conditions, or large ships cannot exceed their hull speed. Thus, the value range of the nine selected influencing parameters was restricted in order to obtain a nine dimensional space non-sparsely filled with wake samples, reducing the risk of curse of dimensionality as well (Figure 1(B.7)). Additionally, the value range of influencing parameters measured in degrees was projected down from 0° – 360° to 0° – 90° . The performed projection is displayed in Figure 3. In this way the complexity of the detectability model is reduced significantly, because only one detectability peak must be modeled, instead of two with reversed direction as in [15]. After discarding all wake samples with influencing parameters outside the defined value range, a training dataset consisting of 2156 labelled wake samples was concluded (Figure 1(B.8)).

Table 1. List of the nine influencing parameters considered in the detectability model along with a description and the value range, in which all samples in the training dataset lie; also a default parameter setting used for the plots in Section 3 is provided.

Influencing Parameter Name	Description	Value Range (Default Setting)
AIS-Vessel-Velocity	Velocity of the vessel derived from AIS messages interpolated to the image acquisition time	0 m/s to 12 m/s (6 m/s)
AIS-Length	Length of the corresponding vessel based on AIS information	10 m to 390 m (100 m)
SAR-Wind-Speed	Wind speed estimated from the SAR background around the vessel using the XMOD-2 geophysical model function [29,33]	2 m/s to 10 m/s (6 m/s)
Incidence-Angle	Incidence angle of the radar cropped to TerraSAR-X's full performance value range	20° to 45° (30°)
SAR-Significant-Wave-Height	Significant wave height estimated from the SAR background around the vessel using the XWAVE_C empirical model function [34]	0 m to 3 m (0.5 m)
SAR-Significant-Wave-Length	Wave length estimated from the SAR background around the vessel using the XWAVE_C empirical model function [34]	75 m to 350 m (150 m)
AIS-CoG-SAR-Wave-Direction	Absolute angular difference between AIS-CoG and wave direction estimated from the SAR background around the vessel using the XWAVE_C empirical model function [34]. The 0°–360° value range has been projected to 0°–90° as displayed in Figure 3.	0° to 90° (45°)
AIS-CoG	The course over ground based on AIS information relative to the radar looking direction (0° means parallel to range and 90° mean parallel to Azimuth). The 0°–360° value range has been projected to 0°–90° as displayed in Figure 3.	0° to 90° (45°)
AIS-CoG-WRF-Wind-Direction	Absolute angular difference between AIS-CoG and wind direction estimated by the Weather Research and Forecasting Model (WRF) [35] nearby the vessel. The 0°–360° value range has been projected to 0°–90° as displayed in Figure 3.	0° to 90° (45°)

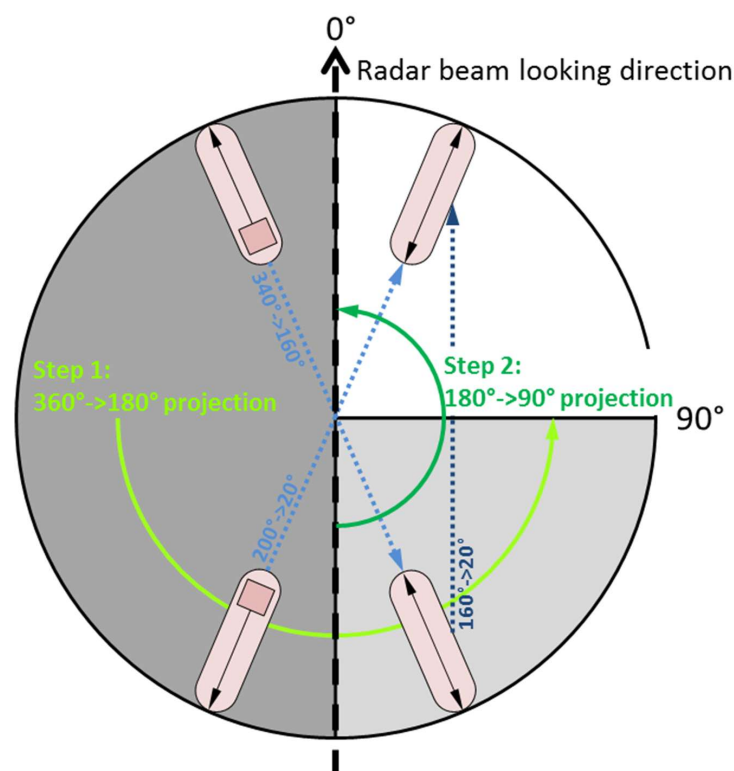


Figure 3. Example for a projection of a ship's heading from 0°–360° down to 0°–90°. The same projection has been applied to all influencing parameters measured in degrees.

3. Results

Figure 1 part C displays, where the procedures and results explained in this section are integrated in the overall workflow executed for this study. In this section the detectability model is detailed and the selection of the best-performing hyperparameters for adjustment of the model's complexity is explained. Further, is explained how the model can be used to visualize the detectability with respect to the influencing parameters. Finally, the model results are displayed and described.

3.1. Tuning of the 9D SVM Detectability Model

In [14] a linear logistic regression classifier was used for binary classification of wake samples with the class labels “detected” or “not detected” based on various combinations of three influencing parameters. The probability of class affiliation to the class “detected” was used to express the probability of detection. The same approach is adopted for this study, but a Support Vector Machine (SVM) classifier is trained on all nine influencing parameters together (Figure 1(C.9)). SVM classifiers have the advantage among other classifiers that they can be easily tuned in their complexity [36]. Actually SVMs are not capable of providing probability estimates of class affiliation, but this drawback is overcome by training the probability estimates after classifier training as proposed in [37]. By only considering the probability estimates of class affiliation to the class “detected”, which is calculated from the nine-dimensional input to the SVM, the model can be expressed by the following simplified formula:

$$PoD = f(x_1, x_2, x_3, x_4, x_5, x_6, x_7, x_8, x_9), \quad (1)$$

where $x_i \forall i \in \{i \in \mathbb{N} | 1 \leq i \leq 9\}$ denotes one of the nine influencing parameters listed in Table 1 using the subscript i as index, f is the SVM detectability model and $PoD \in [0, 1]$ the derived probability of detection.

Using a linear kernel in the SVM is similar to the linear logistic regression classifier approach used in [14]. Multiple settings for hyperparameters of the SVM model were tested for this study. Most of the settings allowed a representation of non-linear influences of the nine selected parameters on the detectability and their interdependencies. It turned out that a polynomial kernel with a degree of two can outperform the linear model. First, a much higher complexity, induced by higher degree of the polynomial kernel or due to radial-basis or sigmoid-kernel, leads to overfitting [36]. Second, for all the nine selected influencing parameters only one detectability peak is expected, therefore a polynomial kernel with a degree of two is sufficient to model this one peaked maximum. Different cost-parameter values ranging from 0.01 to 100 at steps of multiples of 10 were tried and finally a low cost-parameter was set, which allows the SVM model to adopt a large margin and account for the noisy dataset. The gamma-parameter controls the magnitude of curvature of the separating hyperplane. Its tuning is dependent on the cost-parameter, as a narrower margin requires a stronger bending (i.e., a lower gamma-parameter) in case of non-perfectly separable classes and vice-versa. Gamma-parameter values ranging from 0.001 to 0.1 at steps of multiples of 10 were tried, and the best performance was achieved when gamma is set to 0.01 and cost to 0.1. The tuning of the coef0-parameter was performed over the value range of 0 to 1000 at steps of multiples of 10. However the effect of this parameter on the performance turned out negligible. This can be explained by the fact that a polynomial kernel with a degree of two requires less trading off between the first-order and second-order terms of the polynomial, compared to polynomial kernels with higher degrees. More detailed information about tuning of SVM's hyperparameters can be found in [38]. 10-fold-cross validation was applied to quantify the model's performance [39]. The best performing parameterization of the SVM model is given in Table 2, with which a classification accuracy of $\approx 87\%$ is achieved.

Table 2. Settings of the Support Vector Machine (SVM)’s hyperparameters achieving highest 10-fold-cross validation accuracy on the training dataset.

Hyperparameter Name	Value
Kernel type	polynomial
Kernel degree	2
Cost	0.1
Gamma	0.01
Coef0	100

3.2. Visualization of 9D Detectability Model

As the full visualization of a model with nine dimensions is not feasible by two dimensional figures, only extracted views into the model can be presented here. The views are constructed in a way that they visualize the direct dependencies of influencing parameters with the probability of detection and the interdependencies between the influencing parameters also with regard to detectability. This means one view into the model can only display the value range of two influencing parameters (one on the x-axis and one on the y-axis) at a time, when the probability of detection itself is represented by a color-coded scale (quantifying in a restricted manner values on a z-axis). Such views into the model are in the following denoted as 2D detectability charts or 2D charts. By plotting multiples of these 2D detectability charts, each with a different fixed value setting for the influencing parameters not displayed in the chart, the various effects of the influencing parameters on the detectability can be analyzed. This way of visualizing the models was already proposed in [13] and [14] for the data-driven 3D and 4D detectability models. While for the 3D model only one and for the 4D model only two influencing parameters would have to be set to a fixed value in order to obtain one 2D detectability chart, for the demonstrated 9D model seven influencing parameters must be set to a fixed value. Therefore, the investigation of the 9D space required repeated combination of settings for the influencing parameters and repeated plotting and chart interpretation.

The fastest way of producing each required 2D chart was to first sample the whole value range of the 9D dimensional feature space into a 9D matrix (Figure 1(C.10)). Then each 9D sample from the matrix was fed into the SVM model and the probability of class affiliation for the class label “detected” was assigned to the respective sample, expressing the wake detectability for the respective setting (Figure 1(C.11)). Finally, only the 9D matrix of probability estimates needed to be read out by accessing the probability values according to the desired settings of influencing parameters for which the 2D charts were required (Figure 1(C.12)).

3.3. Characteristics of Influences on Wake Detectability

The characteristics of how an influencing parameter affects the detectability can be categorized into four types. The influences of parameters can also vary in dependency to other influencing parameters. Such dependencies between parameters are here called interdependencies. In this section the parameter with index c for which the characteristics are described is denoted as x_c and its value range as I_c . All the respective other parameters x_o with indices $o \in \{i \in \mathbb{N} | 1 \leq i \leq 9 \wedge i \neq c\}$ are in the set $X_{o \neq c}$ and their respective value ranges are denoted I_o .

3.3.1. Influencing Parameters with No Influence on Detectability

When no significant variation of probability of detection is observed for all magnitudes of the characterized influencing parameter over its whole value range in combination with various magnitude settings of respective other influencing parameters, then the characterized parameter is defined as having no influence on the detectability. This means:

$$f'(x_c, X_{o \neq c}) = \frac{\partial f}{\partial x_c} = 0, \forall x_c \in I_c, \forall x_o \in I_o \quad (2)$$

3.3.2. Influencing Parameters with Independent Monotonic Influence on Detectability

Detectability models with a linear basis like the ones presented in [13,14] are only capable of representing independent monotonic influences of parameters on the detectability. Such an independent monotonic influence on detectability can still be observed for the presented non-linear SVM detectability model. The monotonic influence of such parameters is independent from the magnitudes of any other influencing parameters. Therefore, the parameters reach relatively high absolute correlation coefficients. However, the gradient of detectability's variation for these parameters can change with different magnitudes of other influencing parameters, while for a linear model the gradients are constant. This means:

$$f'(x_c, X_{o \neq c}) = \frac{\partial f}{\partial x_c} \leq 0, \forall x_c \in I_c, \forall x_o \in I_o \quad (3)$$

3.3.3. Influencing Parameters with a One-peaked Maximum Influence on Detectability

The benefit of training a polynomial model is best demonstrated by parameters characterized with a one-peaked maximum influence on detectability. For these the probability of detection reaches one maximum at $x_{c,max}$, which is located inside the value range of the influencing parameter's magnitudes. The gradient of detectability's variation switches its sign at this maximum. On either side of the maximum the influence on detectability is monotonic. This means:

$$f'(x_{c,max}, X_{o \neq c}) = \frac{\partial f}{\partial x_c} = 0, \exists x_{c,max} \in I_c, \forall x_o \in I_o \quad (4)$$

and

$$f''(x_{c,max}, X_{o \neq c}) = \frac{\partial f'}{\partial x_c} \neq 0, \exists x_{c,max} \in I_c, \forall x_o \in I_o \quad (5)$$

3.3.4. Influencing Parameters with Interdependent Monotonic Influence on Detectability

The presented more complex model is also capable of representing monotonic influences on the detectability, which are not independent from the other influencing parameters. Such interdependent monotonic influences mean that the influencing parameter's gradient of detectability's variation can switch its sign, when the magnitude combination of other influencing parameters reaches a certain setting $I_{o,turn}$. On either side of this turning point the influence remains monotonic:

$$f'(x_c, X_{o \neq c}) = \frac{\partial f}{\partial x_c} \leq 0, \forall x_c \in I_c, \forall x_o \in I_o \cap I_{o,turn} \quad (6)$$

Such a turning point in the setting of the interdependent other influencing parameters is characterized by either the influence of the characterized parameter showing no effect on detectability (7) or the influence showing an insignificant one-peaked maximum at $x_{c,max}$ over the parameter's value range (8) and (9):

$$f'(x_c, X_{o \neq c}) = \frac{\partial f}{\partial x_c} = 0, \forall x_c \in I_c, \exists x_o \in I_{o,turn} \quad (7)$$

or

$$f'(x_{c,max}, X_{o \neq c}) = \frac{\partial f}{\partial x_c} = 0, \exists x_{c,max} \in I_c, \exists x_o \in I_{o,turn} \quad (8)$$

and

$$f''(x_{c,max}, X_{o \neq c}) = \frac{\partial f'}{\partial x_c} \neq 0, \exists x_{c,max} \in I_c, \exists x_o \in I_{o,turn} \quad (9)$$

3.4. Categorization of Influencing Parameters by Characteristics of Influences

In the following subsections an extract of 2D detectability charts out of all investigated charts is presented. These charts were selected in a representative way so that they provide an insight into the parameter's influences on detectability and the interdependencies between them. The default setting of fixed values for the influencing parameters is given in brackets in the right column of Table 1.

3.4.1. AIS-CoG-WRF-Wind-Direction

AIS-CoG-WRF-Wind-Direction has no effect on the detectability of ship wakes. Figure 4 shows that the probability of detection remains constant for any magnitude of AIS-CoG-WRF-Wind-Direction for each setting of SAR-Wind-Speed and SAR-Significant-Wave-Height.

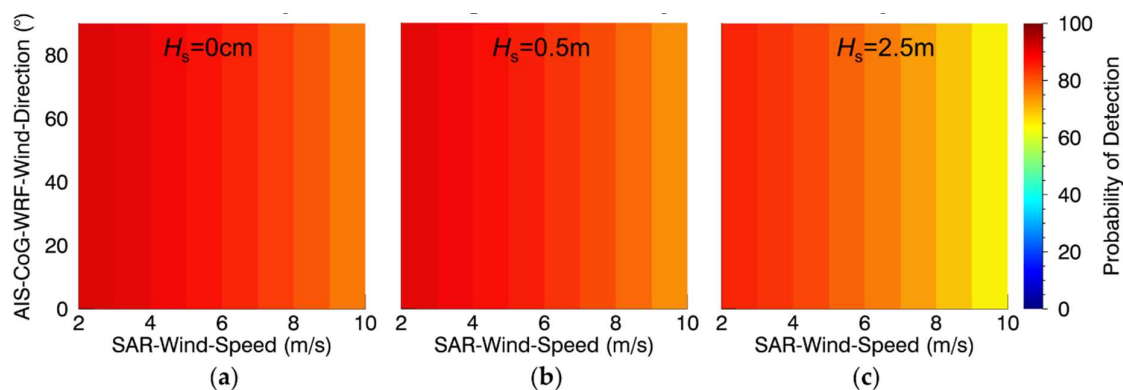


Figure 4. 2D detectability charts based on SAR-Wind-Speed, AIS-CoG-WRF-Wind-direction and from left to right SAR-Significant-Wave-Height with (a) 0 m, (b) 0.5 m, and (c) 2.5 m.

3.4.2. AIS-Vessel-Velocity

AIS-Vessel-Velocity has an independent monotonic influence on detectability. This characteristic can be observed in the Figure 5, but also in the Figures 8 and 9, which are presented later in this section, when AIS-Vessel-Velocity is contrasted with the other two influencing parameters, Incidence-Angle and SAR-Significant-Wave-Length, respectively. Already the relatively high absolute correlation coefficient of this parameter indicates that it is also the parameter with most influence compared to the other influencing parameters. With increasing magnitude of AIS-Vessel-Velocity, the detectability increases.

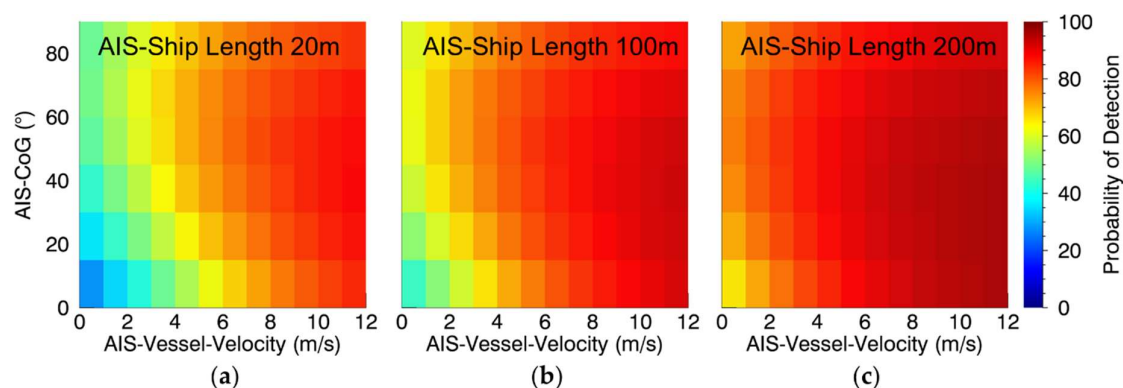


Figure 5. 2D detectability charts based on AIS-Vessel-Velocity, AIS-CoG and from left to right AIS-Length with: (a) 20 m, (b) 100 m, and (c) 200 m.

3.4.3. AIS-Length

Figure 5 also shows that an independent monotonic influence is present for the AIS-Length influencing parameter. With increasing magnitude of AIS-Length, the detectability increases.

3.4.4. SAR-Wind-Speed

The independent monotonic influence of SAR-Wind-Speed on detectability is observable in the Figure 4. With increasing magnitude of SAR-Wind-Speed, the detectability decreases.

3.4.5. SAR-Significant-Wave-Height

The fourth influencing parameter with independent monotonic influence is SAR-Significant-Wave-Height. Its characteristics can be retrieved from Figure 4. With increasing magnitude of SAR-Significant-Wave-Height, the detectability decreases.

3.4.6. AIS-CoG

From Figure 5 a one-peaked maximum influence of AIS-CoG on detectability can be derived. It is located between magnitudes from $\approx 30^\circ$ to $\approx 70^\circ$, interdependently from AIS-Vessel-Velocity. The maximum is located around 30° for low AIS-Vessel-Velocity and shifts towards 70° with increasing AIS-Vessel-Velocity.

3.4.7. AIS-CoG-SAR-Wave-Direction

For AIS-CoG-SAR-Wave-Direction the detectability reaches its one-peaked maximum around magnitudes from $\approx 60^\circ$ to $\approx 70^\circ$, which can be observed in the Figures 6 and 7. The interdependency to other influencing parameters is negligible.

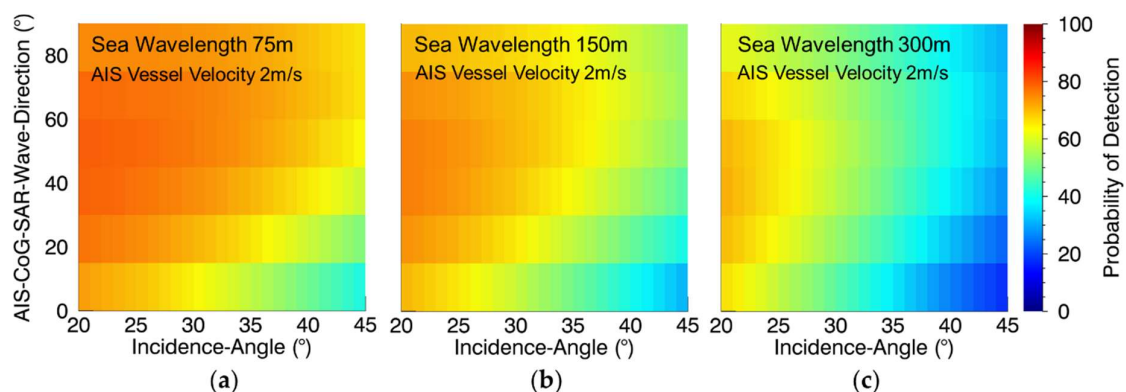


Figure 6. 2D detectability charts based on Incidence-Angle, AIS-CoG-SAR-Wave-direction and from left to right SAR-Significant-Wave-Length with: (a) 75 m, (b) 150 m, and (c) 300 m, deviating from the default setting for this chart AIS-Vessel-Velocity was set to 2 m/s.

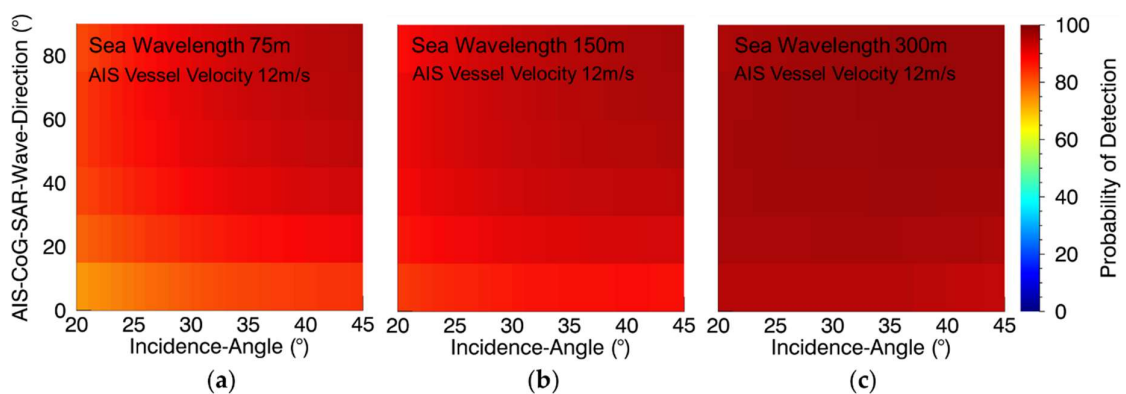


Figure 7. 2D detectability charts based on Incidence-Angle, AIS-CoG-SAR-Wave-direction and from left to right SAR-Significant-Wave-Length with: (a) 75 m, (b) 150 m, and (c) 300 m, deviating from the default setting for this chart AIS-Vessel-Velocity was set to 12 m/s.

3.4.8. Incidence-Angle

Incidence-Angle has an interdependent monotonic influence on wake detectability. Its monotonic influence is interdependent to AIS-Vessel-Velocity, SAR-Wind-Speed and SAR-Significant-Wave-Height. In the 2D detectability charts in Figure 8 the general sea surface roughness characterized by SAR-Wind-Speed and SAR-Significant-Wave-Height is expressed by the Beaufort-Scale number (abbreviated as bft) [40]. In the Figure 6 to Figure 8 the interdependency to AIS-Vessel-Velocity is observable. When describing the influence of Incidence-Angle on detectability, four different combinations with different parameter magnitudes must be considered

- For smooth ocean surface the turning point is located around 9 m/s of AIS-Vessel-Velocity:
 - Below 9 m/s with increasing magnitude of Incidence-Angle, the detectability decreases by few percentage points close to 9 m/s up to ~35 percentage points close to 0 m/s
 - Above 9 m/s no influence of Incidence-Angle on the detectability is observed
- For rough ocean surface the turning point is located around 6 m/s of AIS-Vessel-Velocity:
 - Below 5 m/s with increasing magnitude of Incidence-Angle, the detectability decreases by few percentage points close to 6 m/s up to ~20 percentage points close to 0 m/s
 - Above 5 m/s with increasing magnitude of Incidence-Angle, the detectability increases by few percentage points close to 6 m/s up to ~20 percentage points close to 12 m/s
- This means, the turning point, at which the gradient of detectability's variation of Incidence-Angle switches its sign, decreases from 9 m/s to 6 m/s when the ocean surface gets rougher.

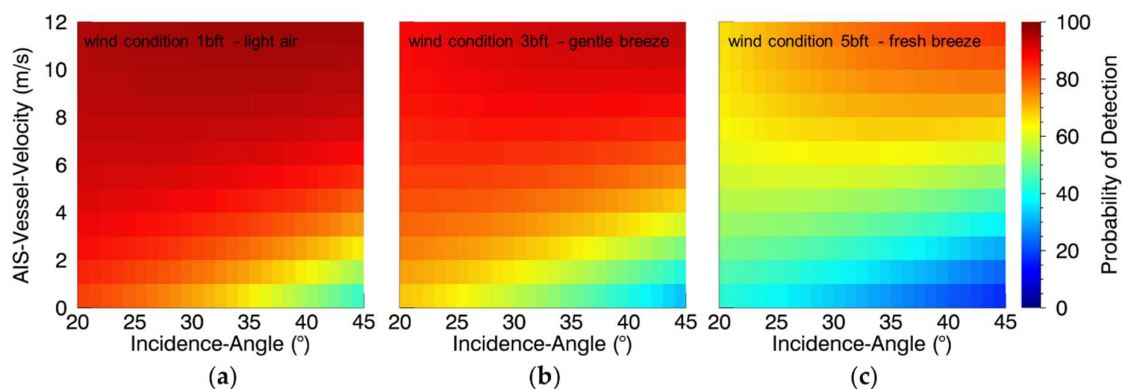


Figure 8. 2D detectability charts based on Incidence-Angle, AIS-Vessel-Velocity and from left to right Beaufort numbers with: (a) 1 bft, (b) 3 bft, and (c) 5 bft.

3.4.9. SAR-Significant-Wave-Length

Also SAR-Significant-Wave-Length has a monotonic influence, which is interdependent from AIS-Vessel-Velocity, SAR-Wind-Speed, and SAR-Significant-Wave-Height. All interdependent monotonic influences are shown in Figure 9. When describing the influence of the SAR-Significant-Wave-Length on detectability, again four different combinations with different parameter magnitudes must be considered

- For smooth ocean surface the turning point is located around 3 m/s of AIS-Vessel-Velocity:
 - Below 3 m/s with increasing magnitude of SAR-Significant-Wave-Length, the detectability decreases by few percentage points close to 3 m/s up to ~10 percentage points close to 0 m/s

- o Above 3 m/s with increasing magnitude of SAR-Significant-Wave-Length, the detectability increases by few percentage points close to 3 m/s up to ~5 percentage points close to 12 m/s
- For rough ocean surface the turning point is located around 6 m/s of AIS-Vessel-Velocity:
 - o Below 6 m/s with increasing magnitude of SAR-Significant-Wave-Length, the detectability decreases by ~5 percentage points close to 6 m/s up to ~25 percentage points close to 0 m/s
 - o Above 6 m/s with increasing magnitude of SAR-Significant-Wave-Length, the detectability increases by few percentage points close to 6 m/s up to ~20 percentage points close to 12 m/s
- This means, the turning point, at which the gradient of detectability's variation of SAR-Significant-Wave-Length switches its sign, increases from 3 m/s to 6 m/s when the ocean surface gets rougher

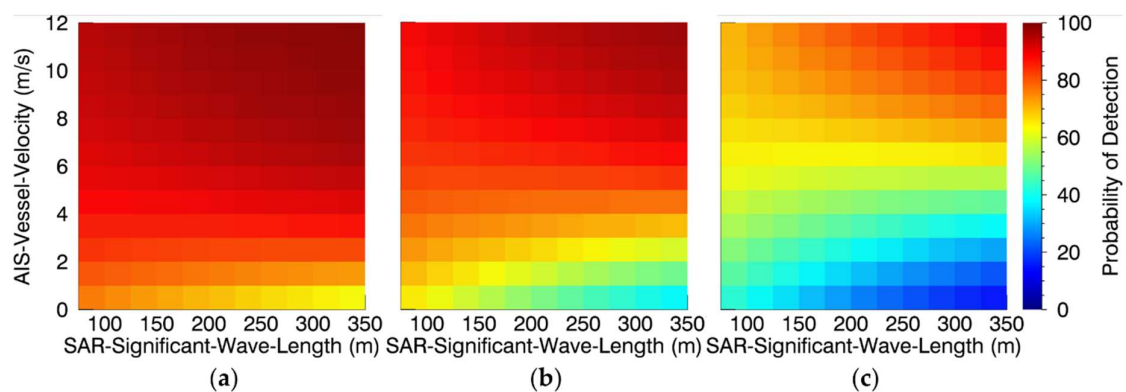


Figure 9. 2D detectability charts based on SAR-Significant-Wave-Length, AIS-Vessel-Velocity and from left to right Beaufort numbers with: (a) 1 bft, (b) 3 bft, and (c) 5 bft.

4. Discussion

The results obtained by the presented detectability model are partially based on influencing parameters retrieved using other models, i.e., the XWAVE_C model for sea state retrieval, the XMOD-2 model for wind speed estimation and the WRF model for estimation of wind direction. Models possess only limited capabilities of representing reality and different measures for accuracy apply for each of them. Therefore, an interesting result of this study is that the detectability model trained on the basis of these imperfect models and real data is able to reproduce many oceanographic expectations stated by other researchers in the past. The accuracies of XWAVE_C and XMOD-2 were also considered in the following discussion.

4.1. AIS-CoG-WRF-Wind-Direction

Hennings et al. [15] found out that the wind direction has a slight influence on the detectability of the Kelvin wake arms. By using the influencing parameter AIS-CoG-WRF-Wind-Direction in the detectability model proposed in this study, this behavior could not be reproduced. First, using the WRF model as a substitute for the actually required high resolution wind direction is insufficient in terms of local wind field variability. Higher resolution wind direction models or an automatic extraction of wind direction from the SAR image is required. Second, the real influence is low and the presented detectability model may also not be sensitive enough to represent this influence or the real influence is interdependent on influencing parameters, which are not considered in this study.

4.2. AIS-Vessel-Velocity

The most pronounced influencing parameter is AIS-Vessel-Velocity. Figure 10 shows wakes for the three different vessel velocity classes: slow with AIS-Vessel-Velocity up to 4 m/s

(Figure 10a), medium with AIS-Vessel-Velocity between 4 m/s and 9 m/s (Figure 10b) and fast with AIS-Vessel-Velocity above 9 m/s (Figure 10c). The differences between these classes are connected with forcing waves of different amplitude, period and propagation. For example, for low speed vessels the Kelvin waves and their SAR signature are weaker than the SAR signatures of turbulent wakes.

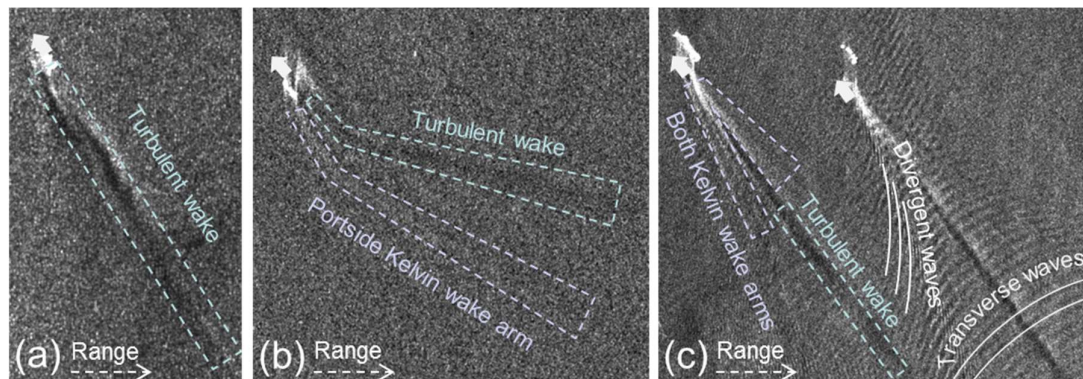


Figure 10. Slow vessel (a), middle speed vessel (b) and high speed vessel (c); for the slow vessel only the turbulent wake is visible, for the middle speed the portside Kelvin wake arm produces a stronger signal, for the high speed vessel the Kelvin wave is steeper producing bright backscatter. All other influencing parameters have comparable setting for the above wake patches. The transvers waves and divergent waves producing the Kelvin wakes arms are clearly observable behind the fast right vessel (c).

Briefly, faster vessels are better detectable as depicted by Figure 5 due to two reasons.

- First, a larger velocity results in a more extensive area of the ocean surface being affected in a shorter time and larger wake signatures are better recognizable.
- Second, the compressed divergent waves are especially well imaged on SAR, because of the steep waves with dense wave crests and high amplitudes forming shapes similar to corner reflectors and also the resulting wave breaking [41,42].

In the following, a detailed explanation is given, why wakes from faster vessels are better detectable. The propagation of wakes is based on the wake's Froude number [43,44], a non-dimensional measure for the wave drag behind the ship calculated using length and velocity of a ship by:

$$Fr = V / \sqrt{gL}, \quad (10)$$

where V is the AIS-Vessel-Velocity, L the AIS-Length and g the gravitational acceleration. The amplitude of the transversal waves decreases for larger Froude numbers and the V-shaped wave pattern becomes narrower due to compressing of the divergent waves when the ship exceeds its hull speed [43,44]. Hence, the radar backscatter resulting from these waves is higher for larger incidence angles and so wakes from fast vessels are better detectable. This is indicated by Figures 7 and 8.

Figures 6 and 8 on the other hand show that for slow vessels lower incidence angles are better for detection, what can be explained as follows. The V-shaped Kelvin envelope with its delimiting constant angle of $\approx 19.47^\circ$ as defined by [45] is visible on SAR due to constructive interference between the wave crests of divergent and transversal waves. The resulting higher amplitude and sometimes wave breaking are only present for small Froude numbers, as the transversal waves vanish for larger Froude numbers so that less constructive interference is present. The backscattering of this effect is low, when compared to the effects occurring with large Froude numbers. Hardly affected by the ship velocity is the turbulent wake, which is represented by a smooth ocean surface originating from the ship's propeller.

Similar to the detection of oil spills, the detection of the ship's turbulent wake is easier with lower incidence angles as the contrast between the smooth wake and the rougher surrounding ocean surface

is more distinct [32]. With higher ship velocity only the extent of the smoothed ocean surface increases, not the smoothness itself. In general the detection of smooth ocean surface areas is more difficult than of the compressed divergent waves. All these different effects finally constitute the reason why an increase of AIS-Vessel-Velocity generally implies a better detectability of wakes. Figure 8 indicates additionally that a distinct change of the wake signature due to larger Froude numbers in most cases is observable with an AIS-Vessel-Velocity between 5 m/s and 9 m/s.

4.3. AIS-Length

Beside the AIS-Vessel-Velocity also the AIS-Length is required for calculation of Froude number. The Froude number is inversely proportional to AIS-Length, but the ascending slope of the Froude number is higher for small magnitudes of AIS-Length, while for large magnitudes the gradient is much smaller. This means small ships have in general larger Froude numbers than large ships. The increased detectability of ship wakes with larger Froude numbers, as explained in Section 4.2, compensates to some degree the fact that large ships produce higher waves, what makes them better detectable. Still, the better detectability of large ships can be observed in Figure 2. When taking into account that an increase of AIS-Length by a factor of 10 from 20 m to 200 m only leads to an increase of detectability of only around 10 percentage points, then the effect of this influencing parameter on detectability is almost negligible, what was already stated in [14].

4.4. SAR-Wind-Speed and SAR-Significant-Wave-Height

The influencing parameters SAR-Wind-Speed and SAR-Significant-Wave-Height are in practice proportionally connected to each other as they both describe the roughness of the ocean surface as a result of striking winds. Wake samples with high SAR-Wind-Speed and low SAR-Significant-Wave-Height (storm formation) or low SAR-Wind-Speed and high SAR-Significant-Wave-Height (only swell) occur rarely in the dataset, especially in the study area North Sea, Baltic Sea and Mediterranean Sea. Thus, in the Figures 8 and 9 both influencing parameters are combined using the Beaufort scale [40]. From Figure 4 a significant decrease of detectability can be observed with increasing SAR-Wind-Speed and also a decrease of detectability with increasing SAR-Significant-Wave-Height is pronounced. First, the rougher ocean conditions interfere with the formation and propagation of all wake components in reality, what means wake signatures can only occur less distinct and smaller. Second, the bright and inhomogeneous appearance of the ocean surface, which is surrounding and superimposing the wake signatures, impedes the unambiguous perception of the respective structures in the images [15].

4.5. AIS-CoG

The propagation direction of cusp waves can be approximated by propagation direction of divergent waves [15]. The detectability of cusp waves forming the Kelvin wave pattern is expected to be sensitive to AIS-CoG as the high amplitudes and breaking waves deploy their best backscattering properties, when exposed perpendicularly by the radar beam contrary to the wave's running direction [15,19,23]. Actually the maximum detectability should then be approached for magnitudes of AIS-CoG around 70.53° . Indeed, two Kelvin arms exist for each wake, but after projection of the ship's heading onto the 0° to 90° value range both arms are projected onto 19.47° , where 70.53° is the projection of the perpendicular direction. Thus, also the information about the respective Kelvin arm's running direction is dropped during the projection of the ship's heading. Figure 5 shows that generally for slow ships and also for fast and small ships the maximum is indeed located around 70° , but for fast and large ships the maximum is around 30° . As explained above, for fast ships the Kelvin wake arms represent the more distinct feature and therefore actually the maximum should be located around 70° especially for fast ships. The maximum around 30° is contradicting here. However, the small gradients around the maximum illustrate that the general dependency of detectability to AIS-CoG is so marginal that inaccuracies in the AIS dataset could lead to false estimations for this condition,

as only few samples of fast and large ships are presents in the data. The maximum around 30° for fast and large ships should therefore be neglected.

4.6. AIS-CoG-SAR-Wave-Direction

The maximum detectability of the influencing parameter AIS-CoG-SAR-Wave-Direction is shifted from $\approx 70^\circ$ towards $\approx 60^\circ$ for different magnitudes of SAR-Significant-Wave-Length as depicted in Figures 6 and 7. The wavelength is directly estimated from SAR subscenes using a 2D fast Fourier transform (FFT) and a consecutive search for the peak wavelength. Cases of non-pronounced imaged wave signatures are not discarded from the dataset and this is recognized to lead to some inaccuracies in the estimation of wavelength. Thus, this shift is also connected to these inaccuracies in wavelength estimation and should be neglected. Similar to AIS-CoG also for the AIS-CoG-SAR-Wave-Direction parameter the projection of the angles leads to a perpendicular angle of ocean waves towards Kelvin wake arms in the magnitude of 70.53° . A peak around 70.53° means that the waves in the two Kelvin wake arms are colliding with the in parallel running ocean surface waves. Already the resulting constructive interference and the in turn resulting heightened wave amplitude and wave breaking increase the backscattering and therefore the wake's detectability. In cases where the in-parallel running waves collide with the Kelvin wake arm's waves in the opposite running directions, this effect is even more intense. Thus, the maximum around 70.53° matches oceanographic expectations.

4.7. Incidence-Angle

According to [15] and [32] Kelvin wake arms and turbulent wake are both less visible under high incidence angle conditions, which is also observable in the Figure 8 for slow AIS-Vessel-Velocity. However, according to Figure 8 for higher AIS-Vessel-Velocity the dependency is reversed, which is an unexpected result regarding oceanographic expectations. This reversed dependency for high AIS-Vessel-Velocity is not documented in the literature, but it is explained in Section 4.1 by the high Froude numbers of fast vessels, which produce high amplitude waves and wave breaking at the Kelvin wake arms.

4.8. SAR-Significant-Wave-Length

Generally, the interaction of wind waves with short wavelengths and steep crests with the ship's wake principally differs from the interaction of waves produced by swell with longer wavelength and smooth crests. The complex dependency of detectability from different magnitudes of SAR-Significant-Wave-Length is best indicated by Figure 9. In general, for short SAR-Significant-Wave-Length the Kelvin wave pattern is less visible. The short waves mean the dominant local steep wind waves, which interfere with the Kelvin wake arms in a destructive manner. Further, the more inhomogeneous, brighter ocean background makes the recognition of the Kelvin wave pattern more difficult. This is also observable in the Figures 6 and 7, where the gradients around the maximum detectability regarding AIS-CoG-SAR-Wave-Direction are more pronounced for short SAR-Significant-Wave-Length compared to long SAR-Significant-Wave-Length, what means less influence of AIS-CoG-SAR-Wave-Direction on detectability for this condition.

In case of swell sea state conditions less or no collisions of ocean waves with the Kelvin wake arms occur, as the swell waves only increase and decrease the general sea surface height without interference [16]. On the contrary, small magnitudes of SAR-Significant-Wave-Length are slightly better for recognizing turbulent wakes, what is indicated by Figure 9 for slow AIS-Vessel-Velocity. The reason is that the darker turbulent wakes have a better contrast to the larger amount of surrounding bright wave crests, which are flattened by the ship's propeller in the wake.

5. Applications

Given the case that a wake has been detected, it is possible to reverse the detectability model in order to derive information about the four missing parameters with independent

monotonic influence on detectability. Three of these, namely AIS-Length, SAR-Wind-Speed, and SAR-Significant-Wave-Height, are available in most of the cases or can directly be derived from the SAR image. Therefore, the model reversion can be used to provide rough estimations of the underlying AIS-Vessel-Velocity, which a moving object must possess as a minimum to produce a detectable wake signature. For the plots in Figure 11, a probability of detection threshold of 80% is defined and the minimum AIS-Vessel-Velocity is derived, for which the model provides a probability of detection above the threshold. Figure 11 also provides a redundant view on the complex dependency of Incidence-Angle as well as SAR-Significant-Wave-Length on AIS-Vessel-Velocity, SAR-Wind-Speed, and SAR-Significant-Wave-Height with regard to detectability.

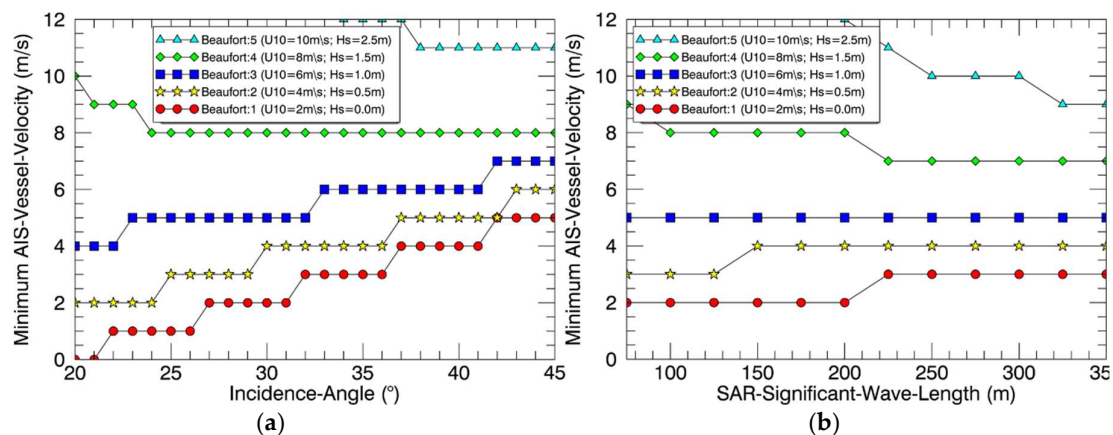


Figure 11. Minimum vessel velocity calculated for the default parameters and changing Incidence-Angle (a) and SAR-Significant-Wave-Length (b) respectively. Results obtained by varying SAR-Wind-Speed and SAR-Significant-Wave-Height are displayed by different line markers. The minimum probability of detection was set to 80%.

Beside the estimation of minimum values for missing parameters, the detectability model can be used to control an automatic wake detection process. Automatic wake detection based on Radon Transform as developed by [5] could be accelerated by limiting the search space in the Radon domain to wake headings, for which a certain level of probability of detection is reached. Also the search for specific wake components may be skipped in case these components are not detectable under certain characteristics of influencing parameters.

6. Conclusions

The linear wake detectability model presented in [14] has been extended by a non-linear basis using a Support Vector Machine classifier with a polynomial kernel of second grade. The model classifies the input data between the classes “detected” and “not detected”, where the probability of class affiliation to the class “detected” is taken as measure for the probability of detection of ship wakes in SAR imagery. Nine influencing parameters, which are affecting the detectability, are considered simultaneously in a single model. Thus, the model can represent not only the dependency of detectability from the influencing parameters, but also depict interdependencies between them. The influencing parameters describe different environmental conditions (i.e., wind speed, wind direction, sea state height, sea state direction and sea state wave length), ship properties (i.e., size, heading, and velocity) and image acquisition settings (i.e., incidence angle, beam looking direction).

Most of the statements about the influencing parameters are theoretically expected, but in this publication they are quantitatively proven using real data. The main outcomes are:

- The higher the vessel velocity the higher the detectability
- The radar beam looking direction and the ocean waves’ traveling direction should be perpendicular to the angle of Kelvin wake arms for higher detectability

- Rough, inhomogeneous ocean surface conditions worsen the detectability
- Slow ships are better detectable with lower incidence angles or shorter wavelengths of ocean surface waves and fast ships are better detectable with higher incidence angles and longer wavelengths of ocean surface waves

Beside the statements about the interdependencies of the different influencing parameters, the presented detectability model can also be applied to control an automatic wake detection system. Another possible application of the model is the estimation of minimum vessel velocities, which must be present in order to make the ship produce a detectable wake signature, by inverting the model and setting a fixed level for probability of detection.

Author Contributions: “conceptualization, B.T.; methodology, B.T.; software, B.T.; validation, B.T.; formal analysis, B.T., A.P. and S.J.; investigation, B.T.; resources, B.T.; data curation, B.T. and D.V.; writing—original draft preparation, B.T.; writing—review and editing, D.V.; visualization, B.T.; supervision, S.J. and D.V.; project administration, S.J.; funding acquisition, S.J.”

Funding: This research received no external funding.

Acknowledgments: TerraSAR-X data has been acquired using the science proposals OCE2203, OCE3207 and OCE3596. The study includes copyrighted material of vesseltracker.com GmbH. The study includes copyrighted material of JAKOTA Cruise Systems GmbH.

Conflicts of Interest: Authors declare no conflict of interest.

References

1. Tings, B.; Bentes, C.; Lehner, S. Dynamically adapted ship parameter estimation using TerraSAR-X images. *Int. J. Remote Sens.* **2016**, *37*, 1990–2015. [\[CrossRef\]](#)
2. Copeland, A.C.; Ravichandran, G.; Trivedi, M.M. Localized Radon Transform-Based Detection of Ship Wakes in SAR Images. *IEEE Trans. Geosci. Remote Sens.* **1995**, *33*, 35–45. [\[CrossRef\]](#)
3. Eldhuset, K. An Automatic Ship and Ship Wake Detection System for Spaceborne SAR Images in Coastal Regions. *IEEE Trans. Geosci. Remote Sens.* **1996**, *34*, 1010–1019. [\[CrossRef\]](#)
4. Crisp, D.J. *The State-of-the-Art in Ship Detection in Synthetic Aperture Radar Imagery*; DSTO Information Sciences Laboratory: Edinburgh, Scotland, 2004.
5. Graziano, M.D.; D’Errico, M.; Rufino, G. Wake Component Detection in X-Band SAR Images for Ship Heading and Velocity Estimation. *Remote Sens.* **2016**, *6*, 498. [\[CrossRef\]](#)
6. Biondi, F. Low-Rank Plus Sparse Decomposition and Localized Radon Transform for Ship Wake Detection in Synthetic Aperture Radar Images. *IEEE Geosci. Remote Sens. Lett.* **2017**, *15*, 117–121. [\[CrossRef\]](#)
7. Biondi, F. (L+ S)-RT-CCD for Terrain Paths Monitoring. *IEEE Geosci. Remote Sens. Lett.* **2018**, *15*, 1209–1213. [\[CrossRef\]](#)
8. Biondi, F. A Polarimetric Extension of Low-Rank Plus Sparse Decomposition and Radon Transform for Ship Wake Detection in Synthetic Aperture Radar Images. *IEEE Geosci. Remote Sens. Lett.* **2018**, *16*, 75–79. [\[CrossRef\]](#)
9. Schurmann, S.R. Radar characterization of ship wake signatures and ambient ocean clutter features. *IEEE Aerosp. Electron. Syst. Mag.* **1989**, *4*, 182–187. [\[CrossRef\]](#)
10. Vachon, P.; Campbell, J.; Bjerkelund, C.; Dobson, F.; Rey, M. Ship Detection by the RADARSAT SAR: Validation of Detection Model Predictions. *Can. J. Remote Sens.* **1997**, *23*, 48–59. [\[CrossRef\]](#)
11. Vachon, P.; Wolfe, J.; Greidanus, H. Analysis of Sentinel-1 marine applications potential. In Proceedings of the 2012 IEEE International Geoscience and Remote Sensing Symposium, Munich, Germany, 22–27 July 2012.
12. Vachon, P.; English, R.; Sandrasegaram, N.; Wolfe, J. *Development of an X-Band SAR Ship Detectability Model: Analysis of TerraSAR-X Ocean Imagery*; Defence R&D Canada: Ottawa, ON, Canada, 2013.
13. Tings, B.; Bentes, C.; Velotto, D.; Voinov, S. Modelling Ship Detectability Depending On TerraSAR-X-derived Metocean Parameters. *CEAS Space J.* **2018**, 1–14. [\[CrossRef\]](#)
14. Tings, B.; Velotto, D. Comparison of ship wake detectability on C-band and X-band SAR. *Int. J. Remote Sens.* **2018**, *39*, 4451–4468. [\[CrossRef\]](#)
15. Hennings, I.; Romeiser, R.; Alpers, W.; Viola, A. Radar imaging of Kelvin arms of ship wakes. *Int. J. Remote Sens.* **1999**, *20*, 2519–2543. [\[CrossRef\]](#)

16. Alpers, W.R.; Ross, D.B.; Rufenach, C.L. On the detectability of ocean surface waves by real and synthetic aperture radar. *J. Geophys. Res.* **1981**, *86*, 6481–6498. [\[CrossRef\]](#)
17. Panico, A.; Graziano, M.D.; Renga, A. SAR-Based Vessel Velocity Estimation From Partially Imaged Kelvin Pattern. *IEEE Geosci. Remote Sens. Lett.* **2017**, *14*, 2067–2071. [\[CrossRef\]](#)
18. Zilman, G.; Zapolski, A.; Marom, M. On Detectability of a Ship's Kelvin Wake in Simulated SAR Images of Rough Sea Surface. *IEEE Trans. Geosci. Remote Sens.* **2015**, *53*, 609–619. [\[CrossRef\]](#)
19. Lyden, J.D.; Hammond, R.R.; Lyzenga, D.R.; Shuchman, R. Synthetic Aperture Radar Imaging of Surface Ship Wakes. *J. Geophys. Res.* **1988**, *93*, 12293–12303. [\[CrossRef\]](#)
20. Reed, A.M.; Milgram, J.H. Ship Wakes and Their Radar Images. *Annu. Rev. Fluid Mech.* **2002**, *34*, 469–502. [\[CrossRef\]](#)
21. Soloviev, A.; Gilman, M.; Young, K.; Brusch, S.; Lehner, S. Sonar Measurements in Ship Wakes Simultaneous with TerraSAR-X Overpasses. *IEEE Trans. Geosci. Remote Sens.* **2010**, *48*, 841–851. [\[CrossRef\]](#)
22. Milgram, J.H.; Peltzer, R.D.; Griffin, O.M. Suppression of Short Sea Waves in Ship Wakes: Measurements and Observations. *J. Geophys. Res.* **1993**, *98*, 7103–7144. [\[CrossRef\]](#)
23. Alpers, W.; Romeiser, R.; Hennings, I. On the radar imaging mechanism of Kelvin arms of ship wakes. In Proceedings of the IEEE International Geoscience and Remote Sensing, Symposium Proceedings, Seattle, WA, USA, 6–10 July 1998.
24. Tunaley, J.K.E.; Buller, E.H.; Wu, K.H.; Rey, M.T. The Simulation of the SAR Image of a Ship Wake. *IEEE Trans. Geosci. Remote Sens.* **1991**, *29*, 149–156. [\[CrossRef\]](#)
25. Gu, D.; Phillips, O. On narrow V-like ship wakes. *J. Fluid Mech.* **1994**, *275*, 301–321. [\[CrossRef\]](#)
26. Stapleton, N.R. Ship wakes in radar imagery. *Int. J. Remote Sens.* **1997**, *18*, 1381–1386. [\[CrossRef\]](#)
27. Thompson, D.R.; Gasparovic, R.F. Intensity modulation in SAR images of internal waves. *Nature* **1986**, *320*, 345–348. [\[CrossRef\]](#)
28. Alpers, W. Theory of radar imaging of internal waves. *Nature* **1985**, *314*, 245–247. [\[CrossRef\]](#)
29. Li, X.-M.; Lehner, S. Algorithm for Sea Surface Wind Retrieval from TerraSAR-X and TanDEM-X Data. *IEEE Trans. Geosci. Remote Sens.* **2014**, *52*, 2928–2939. [\[CrossRef\]](#)
30. Shemdin, O.H. Synthetic Aperture Radar Imaging of Ship Wakes in the Gulf of Alaska. *J. Geophys. Res.* **1990**, *95*, 16319–16338. [\[CrossRef\]](#)
31. Gade, M.; Alpers, W.; Hühnerfuss, H.; Wismann, V.R.; Lange, P.A. On the Reduction of the Radar Backscatter by Oceanic Surface Films: Scatterometer Measurements and Their Theoretical Interpretation. *Remote Sens. Environ.* **1998**, *66*, 52–70. [\[CrossRef\]](#)
32. Minchew, B.; Jones, C.E.; Holt, B. Polarimetric Analysis of Backscatter from the Deepwater Horizon Oil Spill Using L-Band Synthetic Aperture Radar. *IEEE Trans. Geosci. Remote Sens.* **2012**, *50*, 3812–3830. [\[CrossRef\]](#)
33. Jacobsen, S.; Lehner, S.; Hieronimus, J.; Schneemann, J.; Kühn, M. Joint Offshore Wind Field Monitoring with Spaceborne SAR and Platform-Based Doppler LiDAR Measurements. *Int. Arch. Photogramm. Remote Sens. Spat. Inf. Sci.* **2015**, 959–966. [\[CrossRef\]](#)
34. Pleskachevsky, A.; Rosenthal, W.; Lehner, S. Meteorological-marine parameters for highly variable environment in coastal regions from satellite radar images. *ISPRS J. Photogramm. Remote Sens.* **2016**, *119*, 464–484. [\[CrossRef\]](#)
35. Skamarock, W.C.; Klemp, J.B.; Dudhia, J.; Gill, D.O.; Barker, D.M.; Duda, M.G.; Huang, X.-Y.; Wang, W.; Powers, J.G. *A Description of the Advanced Research WRF Version 3*; NCAR Technical Notes; National Center for Atmospheric Research: Boulder, CO, USA, 2008.
36. Berthold, M.; Hand, D.J. *Intelligent Data Analysis—An Introduction*; Springer: Heidelberg, Germany, 2003.
37. Platt, J.C. Probabilistic Outputs for Support Vector Machines and Comparisons to Regularized Likelihood Methods. *Adv. Large Margin Classif.* **2000**, *10*, 61–74.
38. Ben-Hur, A.; Weston, J. A User's Guide to Support Vector Machines. In *Data Mining Techniques for the Life Sciences*; Humana Press: Totowa, NJ, USA, 2010; pp. 223–239.
39. Kohavi, R. A study of cross-validation and bootstrap for accuracy estimation and model selection. In Proceedings of the Fourteenth International Joint Conference on Artificial Intelligence, Montreal, QC, Canada, 20–25 August 1995; Volume 2.
40. Office, M. Beaufort Wind Force Scale. Met Office. 3 March 2016. Available online: <https://www.metoffice.gov.uk/guide/weather/marine/beaufort-scale> (accessed on 20 January 2019).
41. Wackerman, C.; Clemente-Colón, P. Wave Refraction, Breaking and Other Near-Shore Processes. In *Synthetic Aperture Radar*; NOAA NESDIS Office of Research and Applications: Washington, DC, USA, 2000; pp. 171–189.

42. Lehner, S.; Pleskachevsky, A.; Velotto, D.; Jacobsen, S. Meteo-Marine Parameters and Their Variability Observed by High Resolution Satellite Radar Images. *J. Oceanogr.* **2013**, *26*, 80–91. [[CrossRef](#)]
43. Rabaud, M.; Moisy, F. Ship wakes: Kelvin or Mach angle? *Phys. Rev. Lett.* **2013**, *110*, 21. [[CrossRef](#)] [[PubMed](#)]
44. Darmon, A.; Benzaquen, M.; Raphaël, E. Kelvin wake pattern at large Froude numbers. *J. Fluid Mech.* **2014**, 738. [[CrossRef](#)]
45. Kelvin, L. On the waves produced by a single impulse in water of any depth. *Proc. R. Soc. Lond. Ser. A* **1887**, *42*, 80–83.



© 2019 by the authors. Licensee MDPI, Basel, Switzerland. This article is an open access article distributed under the terms and conditions of the Creative Commons Attribution (CC BY) license (<http://creativecommons.org/licenses/by/4.0/>).